

On the modeling of complex 3D bulk metal forming processes via the pseudo-concentrations technique. Application to the simulation of the Mannesmann piercing process

Diego A. Berazategui⁽¹⁾, Miguel A. Cavaliere⁽¹⁾,
Luca Montelatici⁽²⁾ and Eduardo N. Dvorkin^{(1)*}

—
⁽¹⁾Center for Industrial Research, TENARIS
Dr. Simini 250
2804 Campana, Argentina

—
⁽²⁾DalmineTenaris
Piazza Caduti 6 Luglio 1944, 1
24044 Dalmine, Bergamo
Italy

Abstract

The modeling of complex 3D metal forming processes using the flow formulation, implemented via the pseudo-concentrations technique, requires the development of robust computational strategies for dealing with the velocity and pseudo-concentration boundary conditions in the zone where the blank-tools contact is developed. A new algorithm, designed to fulfill those requirements, is presented in this paper.

The Mannesmann piercing process is a metal forming operation used in industry for manufacturing metal seamless pipes. The results of the Mannesmann process finite element simulation are particularly dependent on the accuracy and stability of the algorithm used to describe the contact boundary conditions between the forming tools and the blank. The validation of the finite element model is performed by comparing the numerical predictions obtained using the new algorithm with the results of industrial tests.

*Corresponding author. E-mail: edvorkin@tenaris.com

1 Introduction

For the development of new metal forming processes, for the optimization of existing process set-ups, for the design of forming tools and for predicting the material properties of the metal products that are produced using different manufacturing processes, industry is extensively using nowadays numerical models. In Ref. [1] some of CINI¹ latest developments in this field were discussed.

The flow formulation [2], implemented via the pseudo-concentrations technique [3] [4], has proved to be a very powerful tool for modeling bulk metal forming processes. In previous publications we reported the algorithms that we developed for implementing this technique in our computer code METFOR and we also reported several METFOR applications for the analyses of industrial steel forming processes [5] - [12].

Also, in Ref. [13] the pseudo-concentrations technique was used to develop an elasticity Eulerian formulation.

However, when geometrically involved 3D processes need to be modeled using the pseudo-concentrations technique, numerical difficulties may arise; mostly due to the contact boundary conditions between the blank and the tools. These difficulties for dealing with the contact boundary conditions have been the main obstacle for the diffusion of the pseudo-concentrations technique among the computational mechanics community.

Our purpose in this paper is to discuss a reliable and robust computational algorithm that we implemented for modeling, using the flow formulation implemented via the pseudo-concentrations technique, complex 3D metal forming processes.

To set the framework of our present developments, in the second section of the paper we review the flow formulation implemented via the pseudo-concentrations technique and in the third section we comment on the constitutive relations that we use for modeling hot steel forming processes.

In the fourth section we discuss the new algorithm that we implemented for the solution of complex 3D models.

In the fifth section, in order to validate our numerical developments, we present the simulation of the Mannesmann piercing process. This is a metal forming operation used in industry for the manufacturing of metal seamless pipes. The results of the Mannesmann process finite element simulation are particularly dependent on the accuracy and stability of the algorithm used to describe the contact boundary conditions between the forming tools and the blank. The validation of the finite element model is performed by comparing the numerical predictions obtained using the new algorithm with the results of industrial tests developed in a plant that manufactures seamless steel pipes.

¹CINI is the Center for Industrial Research

2 The flow formulation implemented via the pseudo-concentrations technique

For modeling bulk metal forming processes we implemented an Eulerian formulation in which we use a fixed mesh with the material moving inside it; at each point interior to the mesh we define a variable named *pseudo - concentration* (c).

For the cases with only one free surface we use:

$f_1 \leq c \iff$ there is material at the point,

$f_1 > c \iff$ there is no material at the point,

we can define

$$g(c) = (c - f_1) \quad (1)$$

For the cases with two free surfaces (e.g. inner and outer) we use:

$f_1 \leq c \leq f_2 \iff$ there is material at the point,

$f_1 > c$ or $c > f_2 \iff$ there is no material at the point,

and considering that $f_1 < f_2$ we can define

$$g(c) = (c - f_1)(f_2 - c) \quad (2)$$

For both cases if $g(c) \geq 0$ there is material at the point and if $g(c) < 0$ there is not.

Being (\underline{u}) the velocity field inside the mesh, the c -distribution fulfils the following equations [12]:

$$\underline{u} \cdot \underline{\nabla} c = 0 \quad (\text{stationary problems}) \quad (3a)$$

$$\frac{\partial c}{\partial t} + \underline{u} \cdot \underline{\nabla} c = 0 \quad (\text{transient problems}) \quad (3b)$$

For modeling the metal behavior we use a rigid - viscoplastic constitutive relation; the material flow is described using a viscoplastic associated von Mises model and therefore the metal flow is modeled as incompressible [14].

In our finite element formulation we impose the incompressibility constraint with an augmented Lagrangian technique [11].

Equilibrium is reached using an iterative procedure. In the same iterative loop we solve the nonlinearities coming from the constitutive model and make the augmentation procedure. The equations for the k -th equilibrium iteration, obtained using the Principle of Virtual Work and the augmented Lagrangian technique are [11]:

$$\begin{aligned}
& \int_V 2 \mu^{(k-1)} \Delta \dot{\varepsilon}'_{ij} \delta \Delta \dot{\varepsilon}'_{ij} dv + \int_V \varkappa \Delta \dot{\varepsilon}_v \delta \Delta \dot{\varepsilon}_v dv = \\
& \int_V f_i^v \delta \Delta \dot{u}_i dv + \int_{S_\sigma} t_i \delta \Delta \dot{u}_i dv - \\
& \int_V s_{ij}^{(k-1)} \delta \Delta \dot{\varepsilon}'_{ij} dv - \int_V (p^{(k-1)} + \varkappa \dot{\varepsilon}_v^{(k-1)}) \delta \Delta \dot{\varepsilon}_v dv
\end{aligned} \tag{4}$$

and,

$$\dot{u}_i^{(k)} = \dot{u}_i^{(k-1)} + \Delta \dot{u}_i^{(k)} \tag{5a}$$

$$\dot{\varepsilon}'_{ij}{}^{(k)} = \dot{\varepsilon}'_{ij}{}^{(k-1)} + \Delta \dot{\varepsilon}'_{ij}{}^{(k)} \tag{5b}$$

$$\dot{\varepsilon}_v^{(k)} = \dot{\varepsilon}_v^{(k-1)} + \Delta \dot{\varepsilon}_v^{(k)} \tag{5c}$$

$$p^{(k)} = p^{(k-1)} + \varkappa \dot{\varepsilon}_v^{(k)} \tag{5d}$$

In the above equations,

s_{ij} : deviatoric stress components,

p : hydrostatic stress component,

$\dot{\varepsilon}'_{ij}$: deviatoric strain-rate components (viscoplastic strain-rate tensor),

$\dot{\varepsilon}_v$: volumetric strain-rate component (it is constrained to be zero),

\varkappa : penalty parameter.

The advantage of the augmented Lagrangian procedure over a standard penalty procedure is the possibility of using smaller values for the penalty parameter, obtaining therefore better conditioned matrices. In Ref. [11] we presented several numerical examples in which we showed the better performance of the augmented Lagrangian procedure as compared with the standard penalty procedure,

μ : viscosity, derived using the constitutive viscoplastic relation [2]. For a rigid - viscoplastic material we get,

$$\mu = \frac{\sigma_y(\bar{\varepsilon}, \dot{\varepsilon}, T)}{3 \dot{\varepsilon}} \tag{6}$$

σ_y : instantaneous yield stress, to be discussed in the third section of this paper.

$\dot{\varepsilon}$: material derivative of the equivalent viscoplastic strain.

$$\dot{\varepsilon} = \left(\frac{2}{3} \dot{\varepsilon}_{ij} \dot{\varepsilon}_{ij} \right)^{\frac{1}{2}} \tag{7}$$

$$\dot{\bar{\varepsilon}} = \frac{D \bar{\varepsilon}}{D t} = \frac{\partial \bar{\varepsilon}}{\partial t} + \underline{\dot{u}} \cdot \nabla \bar{\varepsilon} \quad (8)$$

f_i^v : external forces acting on the body, per unit volume of the spatial configuration,

t_i : external surface forces acting on the body,

V : volume of the body spatial configuration ($g(c) > 0$). However, in order to be able to integrate over the complete mesh, at those points where $g(c) < 0$ we use a reduced viscosity value to be discussed in the fourth section of this paper (fictitious material).

S_σ : external surface where loads are prescribed.

With Eqn.(5d) we iteratively build the pressure field using the augmented Lagrangian technique.

For the discretization of the equilibrium equations (4) we use finite elements based on the method of *mixed interpolation of tensorial components*. For 2D problems we use the *QMITC-3F* quadrilateral element, which was described in Ref. [11] and for 3D problems we use the *(H1-P0)-3F* element described in Ref. [9]. Both element formulations fulfil the following requirements:

- They satisfy Irons' Patch Test.
- They do not contain spurious zero energy modes.
- They do not lock due to the incompressibility constraint.

For the discretization of the transport equations (3a or 3b) we use standard isoparametric elements: quadrilateral (Q_1) elements for the 2D problems and hexahedral (H_1) elements for the 3D problems. In all cases, for solving the advective transport equations we use the SUPG technique [15] - [17].

The equivalent viscoplastic strains are obtained integrating the following equations [12],

$$\underline{\dot{u}} \cdot \nabla \bar{\varepsilon} = \frac{\langle g(c) \rangle}{|g(c)|} \dot{\bar{\varepsilon}} \quad (\text{stationary problems}) \quad (9a)$$

$$\frac{\partial \bar{\varepsilon}}{\partial t} + \underline{\dot{u}} \cdot \nabla \bar{\varepsilon} = \frac{\langle g(c) \rangle}{|g(c)|} \dot{\bar{\varepsilon}} \quad (\text{transient problems}) \quad (9b)$$

where $\langle \alpha \rangle = 0$ for $\alpha \leq 0$ and $\langle \alpha \rangle = \alpha$ for $\alpha > 0$ (Macauley brackets)

Since in our Eulerian formulation the material moves inside a fixed mesh:

- The formulation directly provides the free surfaces ($c = f1$ and $c = f2$) in stationary and transient problems.

- The formulation does not require a remeshing algorithm, usually needed when using Lagrangian or Eulerian - Lagrangian formulations [18].

The modeling of the contact problem between the blank and the tools requires a special discussion and is the subject of the fourth section of this paper.

For modeling the friction between the tools and the steel blank we use either a constant friction law or a Coulomb friction law [19] and we apply friction loads only at the segments of the tools-blank interface where actual material is present ($g(c) \geq 0$). When the Coulomb friction is used, the checkerboard effect on the pressure prediction is filtered out using the nodal equivalent loads instead of the contact segment normal stresses [20].

The material viscosity for the fictitious material ($g(c) < 0$) is modeled as,

$$\mu^{g(c)<0} = \frac{\mu^{g(c)>0}}{k_{g(c)<0}} . \quad (10)$$

In the above equation $\mu^{g(c)>0}$ is calculated using Eqn.(6) and $k_{g(c)<0}$ should be, in principle, as large as possible ($\mu^{g(c)<0} = 0$ is the ideal value but it would produce a singular problem; hence we need to have a value of $\mu^{g(c)<0}$ as small as possible but not zero). In our previous publications we have used $k_{g(c)<0} = 10^3$; however, in this paper we introduce a progressive approach in order to improve the convergence of the algorithm. In the fourth section we discuss this approach.

3 Constitutive relations for modeling hot bulk forming processes

When modeling hot metal forming processes using rigid-viscoplastic material models we use an associate viscoplastic flow rule with von Mises yield function [14]. An isotropic hardening law is normally used to relate the instantaneous yield stress (σ_y) with the equivalent viscoplastic strain ($\bar{\epsilon}$), the equivalent viscoplastic strain-rate ($\dot{\bar{\epsilon}}$) and the temperature (T),

$$\sigma_y = \sigma_y(\bar{\epsilon}, \dot{\bar{\epsilon}}, T) . \quad (11)$$

For defining the above relation we can follow two main approaches:

- *Phenomenological constitutive relations.* Curve fitting of simple mechanical tests are used to determine the material parameters involved in these constitutive relations (e.g. torsion, tension or compression tests).
- *Constitutive relations based on the modeling of the microstructural evolution.* These constitutive relations are based on more fundamental physical principles and the material parameters to be adjusted are determined via microstructural observations in programmed temperature - deformation excursions.

In the present section, with focus on the modeling of steel hot forming processes, we will discuss three different phenomenological hardening laws and we will comment on their limitations to accurately represent the behavior of a steel blank being deformed at high temperature.

An inverse calculation algorithm for identifying the material parameters from the results of a simple tests (e.g. the torsion test) was discussed in Ref. [1].

3.1 Phenomenological constitutive relations

In this section we will concentrate our discussion on three strain hardening models: The Fields - Backofen model and two exponential-power models.

- *The Fields - Backofen model*

$$\sigma_y = A(T) \bar{\varepsilon}^{n(T)} \dot{\bar{\varepsilon}}^{m(T)}. \quad (12)$$

This model provides, for a fixed temperature and a fixed viscoplastic strain-rate, a yield stress that monotonically grows with the equivalent viscoplastic strain; hence, it cannot represent recrystallization phenomena ([19], [21]) such as the one illustrated in Fig. 1 for a set of compression tests performed at elevated temperature on steel samples [22].

For each material and for each temperature level to be considered we have to determine the constants $A(T)$, $n(T)$, $m(T)$ for the temperature range of interest.

- *Exponential-power law 1*

$$\sigma_y = [A(T) e^{-B(T)\bar{\varepsilon}} (\bar{\varepsilon} + \bar{\varepsilon}_o)^{n(T)} + C(T) (1 - e^{-B(T)\bar{\varepsilon}})] \dot{\bar{\varepsilon}}^{m(T)}. \quad (13)$$

This law takes the functional form,

$$\sigma_y = f(\bar{\varepsilon}, T) h(\dot{\bar{\varepsilon}}). \quad (14)$$

For a test at constant temperature and constant strain-rate, since $h(\dot{\bar{\varepsilon}}) \neq 0$, the maximum stress (see Fig. 1) will be located at a strain value $\bar{\varepsilon}^*$ given by the following equation,

$$\frac{\partial f}{\partial \bar{\varepsilon}} = 0 \quad (15)$$

therefore, $\bar{\varepsilon}^*$ will not be a function of $\dot{\bar{\varepsilon}}$. This behavior does not match the experimental evidence shown in Fig. 1, from which it is clear that the strain value that defines the stress peak ($\bar{\varepsilon}^*$) grows with the strain-rate. Even though a definition of a constitutive relation that can accommodate the relation $\bar{\varepsilon}^* = \bar{\varepsilon}^*(\dot{\bar{\varepsilon}})$ is most desirable, the above defined exponential-power law has proven to provide very good results in the modeling of many hot bulk forming processes.

For each material and for each temperature level to be considered we have to determine the material constants $A(T)$, $B(T)$, $C(T)$, ε_o , $n(T)$, $m(T)$ for the temperature range of interest.

We also define the following temperature dependence:

$$\begin{aligned}
A(T) &= K_o e^{\frac{\beta}{T}} \\
B(T) &= (r_o + r_1 T) \\
C(T) &= K_{st} e^{\frac{\beta_{st}}{T}} \\
n(T) &= n_o \\
m(T) &= m_o + m_1 T
\end{aligned} \tag{16}$$

- *Exponential-power law 2*

$$\sigma_y = [A(T) e^{-B(T)\bar{\varepsilon}} \sqrt{(1 - e^{-n(T)(\bar{\varepsilon} + \bar{\varepsilon}_o)}) + C(T) (1 - e^{-B(T)\bar{\varepsilon}})] \bar{\varepsilon}^{m(T)}. \tag{17}$$

For this case we have the same comments as for the previous one. We also define the same temperature dependence as for the *exponential-power law 1*.

In Fig. 2 we show the experimental results obtained in a torsion test. Post-processing these experimental results, as discussed in [1], we get the material parameters indicated in Tables I to III.

$A(T)$	74.71 MPa
$n(T)$	0.07
$m(T)$	0.18

Table I. Field-Backofen material parameters for the material in Fig. 2

K_o	104.07 MPa
β	693.77 °K
r_o	-22.32
r_1	0.0187 $\frac{1}{\circ K}$
K_{st}	1.11 MPa
β_{st}	5598.60 °K
m_o	0.055
m_1	$8.58 \cdot 10^{-5} \frac{1}{\circ K}$
n_o	0.64
n_1	0.00 $\frac{1}{\circ K}$
ε_o	0.00

Table II. Exponential-power law 1 material parameters for the material

in Fig. 2

K_o	30.58 MPa
β	3715.72 °K
r_o	-18.51
r_1	0.0157 $\frac{1}{\circ K}$
K_{st}	1.11 MPa
β_{st}	5598.60 °K
m_o	0.055
m_1	$8.58 \cdot 10^{-5} \frac{1}{\circ K}$
n_o	0.10
n_1	0.00 $\frac{1}{\circ K}$
ε_o	0.00

Table III. Exponential-power law 2 material parameters for the material in Fig. 2

In Fig. 2 we also present the approximations to the experimental torque-turn results obtained using the three material laws.

4 The new computational algorithm

The main difficulty in the implementation of the flow formulation via the pseudo-concentrations technique is the proper handling of the velocity and pseudo-concentration contact boundary conditions between the blank and the forming tools.

In what follows we first analyze a simple approach that has been quite successful in the modeling of problems like hot rolling of flat steel products but that has failed to provide reliable and robust results in the modeling of geometrically more complex problems (e.g. the Mannesmann process that we discuss in the next section). Then we present the new algorithm that we developed.

4.1 A simple approach

4.1.1 The equilibrium equation boundary conditions

A first approach for modeling the contact problem between the blank and the forming tool is quite obvious and has been introduced in [12]: the c -dependent boundary conditions.

For \dot{u}_n , the velocity component normal to a tool surface, we use:

$$g(c) < 0 \implies \dot{u}_n = free \quad (18a)$$

$$g(c) \geq 0 \implies \dot{u}_n = 0 \quad (18b)$$

However, during the iterations the boundary condition (18b) is removed if it produces a non-physical traction between the contacting bodies.

4.1.2 The c -transport equation boundary conditions

When a node at the boundary is opened and there is an out-going velocity no boundary conditions have to be enforced; but when there is an in-going velocity the boundary condition has to be enforced, and this is not an obvious task: if we specify an arbitrary nodal value of c , such that $g(c) < 0$, we introduce in the numerical model a locally steep c -distribution that will deteriorate the numerical results produced by integrating Eqns. (3a or 3b).

We have implemented two alternative solution schemes for this problem:

1. The problem domain is enlarged and the contact surface is embedded in it. At the added nodes we fix a value of $c : g(c) < 0$. Therefore when the contact surface is closed we have $g(c) \geq 0$ on one of its sides and $g(c) < 0$ on the other side and when it is opened we have $g(c) < 0$ on both sides (see Fig. 3). This technique was first presented in [9].
2. The problem domain is enlarged and the contact surface is embedded in it. When the boundary velocity is in-going, we zero its component normal to the boundary for the solution of the c -transport equation. This technique was introduced in [23] and we are now using it on a routine basis.

In Fig. 4 we represent a typical analysis developed with the above described formulation: we appreciate the mesh areas with actual material ($g(c) \geq 0$) and with fictitious material ($g(c) < 0$) and also the rolls on which the rolled plate develops frictional contact conditions.

4.2 Our new algorithm

For complex 3D models the above strategies fail to provide convergent solutions; hence, we have developed the new algorithm that we describe in what follows.

4.2.1 Contact definitions

We define the contact surfaces on the forming tools using arcs, as shown in Fig. 5. Each arc is defined by an ordered list of nodes; the order follows the flow direction on the tool (Fig. 6). In the figure, the arc segments between nodes ($J1$) and ($J2$) are *active segments*, that is to say, the blank is actually contacting the forming tool and therefore a boundary condition of zero normal velocity is imposed.

4.2.2 Iterative scheme

In Fig. 7 we present the flow chart of the iterative cycle that we have heuristically developed. The general description of the three levels iterative loop is:

Level 1: equilibrium fulfillment At this level we iteratively solve for equilibrium using Eqns. (4, 5a - 5d) under the following conditions:

- We keep constant the definition of active / non-active contact segments.
- We keep constant the c -distribution.
- We update the equivalent viscoplastic strains with Eqns. (9a or 9b) and therefore the material yield stress with Eqn. (11)

We obtain from this level a velocity field ${}^t\dot{\underline{u}}^{L1}$ using pre-defined convergence tolerances [24].

Level 2: contact conditions update This level is schematically shown in Fig. 8, and we go through the following steps:

- For each arc we check the normal stress on each active segment. When non-physical tensile normal stresses are detected an opening of active segments is performed (see A.1 in the Appendix)
- Starting with the velocity calculated in the previous level we solve Eqns. (3a or 3b) using the second set of boundary conditions from the two discussed in section 4.1.2. The obtained *pseudo-concentrations* distribution is an auxiliary one and we call it $c2$ -distribution.
- We correct the resulting contacts distribution to keep the material balance. (see A.2 and A.3 in the Appendix)

If the number of changes in the nodal contact conditions (NC) is larger than a predefined number ($NCMAX$) when we exit this level we go back to Level 1; otherwise we proceed to Level 3.

Level 3: material properties distribution update When we go through level 2 of the new algorithm and we only introduce a minor change in the nodal contact conditions ($NC < NCMAX$) we exit to level 3 (Fig. 8). We define the last $c2$ -distribution calculated in the previous level to represent the actual c -distribution.

If there are “holes” with $g(c) < 0$ immediately below the active contact surface we cannot apply the friction loads; hence, for the purpose of calculating the friction loads we “fill” those holes.

As we discussed above the viscosity of the material in the areas where $g(c) < 0$ has to be much smaller than the viscosity of the actual material. In order to improve the convergence of the algorithm each time we go through this level we use a larger value of $k_{g(c)<0}$.

For checking the final convergence of the iterative loop we use a velocity norm and convergence is achieved if,

$$\left\| \Delta \dot{\underline{u}} \right\|_2 \leq VTOLA \quad (19)$$

where $\|\Delta \underline{u}\|_2$ is the norm of the incremental velocity field between two consecutive passes through Level 3 and $VTOLE$ is a pre-defined tolerance.

In Fig. 9 we show the flowchart for this level.

5 Modeling of the Mannesmann piercing process

In Fig. 10 we present a scheme of this process used in the production of steel seamless pipes starting from solid continuous casted bars (see Refs. [25] to [30]).

There are many important aspects to be considered to understand this process:

- At the piercer inlet we have a solid bar but at the piercer exit the bar is hollow.
- The central hole is not pierced by the plug: it is formed at the bar center where the material is weakened by the rotating system of orthogonal tensile / compressive stresses induced by the rolling in the convergent zone of the biconical rolls (Mannesmann effect) [31] [32]. A pipe can be produced even without the plug²; but, in this case, the central hole will have an irregular star-like shape rather than the desirable smooth round one. The plug function is to guide the material after the Mannesmann effect and to prevent the oxidation of the new inner surface. In Fig. 11 we present a photograph of a bar that was stopped inside the piercing mill and afterwards cut through a generatrix: it is possible to observe the Mannesmann effect ahead of the plug.
- The plug is conveniently located in advance of the section where the Mannesmann effect produces the first macroscopic hole in the bar center, to prevent an spontaneous (not guided) hole to develop but not too much in advance to prevent the destruction of the plug.
- The bar is heated at approximately $1250^\circ C$ before entering the piercing process, it is extremely important that the center of the bar is as close as possible to the hottest (weakest) point because the hole is going to be localized at this weakest point and we want to reduce the hollow bar eccentricity as much as possible [33].

Several research endeavors have been reported, in which the finite element modeling of the piercing processes was attempted [34] - [38]; however, there is still plenty of room for new contributions in this field.

In what follows we will attempt to model the Mannesmann process, using our finite element code METFOR enhanced with the new algorithm discussed in the previous section.

²As a matter of fact, the Mannesmann brothers discovered the process trying to roll solid bars and getting unwanted "pipes" (Germany, 1880).

The following simplifying assumptions are used in the model:

- I. Isothermal analysis. We shall consider an uniform temperature of $1200^{\circ}C$ – $1250^{\circ}C$ and the corresponding material properties.
- II. We shall not predict the Mannesmann effect but rather use a crude approximation considering a “damaged cone” in front of the plug with a height $L_{Mannesmann}$ (Fig. 12). Inside the cone the material viscosity is multiplied by 0.01.
- III. In the grip zone of the rolls (Fig. 10) there is perfect sticking between the material and the rolls. In the other contact areas we use Coulomb friction.
- IV. The torsional equilibrium of the plug is not considered; hence, we consider on the plug axial friction and free sliding in the circumferential direction.

The developed finite element model will be validated by comparing its numerical predictions with experimental determinations carried out at the piercing mill of TenarisDalmine in Italy.

With the validated model we will perform two sets of analyses:

- To investigate the robustness of the model we shall perform several analyses considering different algorithm parameters and model coefficients. We shall consider that the model is robust only if we can choose the different numerical parameters within an ample range without significantly altering the results.
- To investigate the physics of the piercing process, we shall investigate the changes that are induced in the process output by changes in the process parameters.

5.1 Model validation

In this subsection we discuss the validation of the developed finite element model. This validation is performed by comparing the finite element predictions with the results of industrial tests.

The cases described in Fig. 13 are analyzed.

The three cases correspond to the piercing of bars made with the same steel; the torque-turn curves of this steel are presented in Fig. 14. Post-processing these experimental results we get the material parameters corresponding to the exponential-power law 2 (Table IV).

The isothermal analyses were performed considering a temperature of $1200^{\circ}C$.

K_o	21.59 MPa
β	3374.39 °K
r_o	-48.06
r_1	0.0398 $\frac{1}{\circ K}$
K_{st}	0.16 MPa
β_{st}	8124.72 °K
m_o	0.26
m_1	$-2.76 \cdot 10^{-5} \frac{1}{\circ K}$
n_o	0.70
n_1	0.00 $\frac{1}{\circ K}$
ε_o	0.00

Table IV. Material parameters used in the finite element simulations (Exponential-power law 2)

5.1.1 Cases 1 and 2

Using different plug profiles two industrial tests were performed. In both cases the piercing process was interrupted with the blank inside the machine [39] [40].

In Figs 15 and 16 we present the finite element meshes used for the analyses.

A very sensitive parameter for comparing the numerical and industrial results is the pitch of the helix where the points initially on a straight bar generatrix get located on the final hollow. This torsion helix is an important factor affecting the total redundant deformations that are introduced in the material by the piercing process [25] [30].

For determining the final position of particles originally on a straight generatrix, once the velocity field is determined we integrate it using a fourth order Runge-Kutta procedure and a regular mesh that circumscribes the finite element mesh. Then in Fig. 17 we show the interpolation of an helix passing through the final position of particles that, in the initial bar, were on a straight bar generatrix.

In Table V we compare the numerical and experimental results for the two plug profiles. Of course these results were obtained using a set of friction factors, $L_{Mannesmann}$ values and algorithm parameters. In the following subsection we will investigate how these modeling decisions affected the model results.

Plug	Elements	d.o.f.	FEM - Pitch	Exp. - Pitch
1	96,576	314,097	1158 mm	1054 mm
2	100,950	327,444	714 mm	695 mm

Table V. Comparison between numerical and experimental results

In Figs. 18 and 19 we display the equivalent viscoplastic strains that are introduced by the first plug design and the equivalent viscoplastic strain rates for the case of the second plug design.

In Fig. 20 we compare, for the plug profile # 1, the first fourteen transversal cross sections determined with the model and the corresponding cross sections obtained during the industrial experiment.

5.1.2 Case 3

In this case the piercing process was also interrupted with the blank inside the machine. In Fig. 21 we present the finite element mesh used for the analysis.

The outer surface of the semi-processed bar was mapped using the equipment described in Ref. [41]; the inner surface shape was replicated using a resin cast and the shape of the replica was also mapped as described in Ref. [41]. In Fig. 22 we show the mapping of the outer surface and in Fig. 23 the mapping of the resin cast that replicates the inner surface of the interrupted hollow.

In Figs. 24 and 25 we present, for this case, the comparison between the finite element determined and experimentally mapped surfaces. In these figures we also plot the numerically calculated viscoplastic strains.

Finally in Fig. 26 we show the actual and finite element predicted contact area between the rolls and the bar.

5.2 Sensitivity analyses

In this subsection we will present the results of two sensitivity analyses: sensitivity with respect to the model coefficients and sensitivity with respect to the algorithm parameters.

5.2.1 Sensitivity with respect to model coefficients

We investigate the influence on the numerical solutions of the different coefficients introduced for the modeling of the Mannesmann piercing process.

In Table VI we summarize the results for the different friction coefficients and different values of $L_{Mannesmann}$:

Plug	μ_{rolls}	μ_{shoes}	μ_{plug}	$L_{Mann.}$	FEM-pitch	$\frac{FEM \text{ pitch}}{Exp. \text{ pitch}}$
1	0.2	0.2	0.35	150 mm	1054 mm	0.88
1	0.5	0.2	0.35	150 mm	1252 mm	1.05
1	0.2	0.2	0.35	300 mm	1158 mm	0.97
2	0.2	0.2	0.35	150 mm	695 mm	0.88
2	0.5	0.2	0.35	150 mm	899 mm	1.14
2	0.2	0.2	0.35	300 mm	714 mm	0.90

Table VI. Parametric analysis: friction coefficients and $L_{Mannesmann}$

We conclude that in both cases changing the explored parameters within the ranges shown in Table VI produces an uncertainty in the pitch prediction of approx. $\pm 10\%$.

5.2.2 Sensitivity with respect to algorithm parameters

The value of $DTOL$ (see Appendix) controls the accuracy of our contact conditions representation and, of course, it has to be related to the element sizes.

We run three analyses of the case indicated in Fig. 13 as “*plug profile # 2*” using the $DTOL$ values indicated in Table VII:

	Plug	Rolls	Shoes
Analysis 1	6 mm	6 mm	2 mm
Analysis 2	4.8 mm	4.8 mm	1.6 mm
Analysis 3	3.8 mm	3.8 mm	1.3 mm

Table VII. $DTOL$ values

In Fig. 27 we represent the behavior of the three analyzed cases during the iterative process. It is clear that:

- The three cases converge
- The helix pitch moves in the same direction each time we lower $DTOL$.

5.3 Parametric analyses

In order to demonstrate the usefulness of the developed finite element model as an engineering tool for the analyses of process conditions, we analyze the piercing of a 362 mm bar using the same forming tools but with a different rolls angle γ (Fig. 10). In Table VIII we summarize the angle used for each case and the resulting pitches.

	γ	FEM-pitch
Case A	9°	1771 mm
Case B	7°	1369 mm

Table VIII. Parametric analyses

From the results in Fig. 28 it is evident than when the angle γ diminishes, the viscoplastic work on the pipe increases.

In Fig. 29 we see, for the 7° case, the tensile stresses in front of the plug in an axial section through the shoes.

6 Conclusions

The flow formulation implemented in an Eulerian approach via the pseudo-concentrations technique can be developed into an efficient engineering tool for simulating metal forming processes if the difficulties in modeling the contact conditions between the forming tools and the blank are overcome. The ability to provide an accurate description of these contact conditions is of utmost importance in the modeling of many complex 3D metal forming operations; in particular in the modeling of the Mannesmann process.

In this paper we developed a new contact algorithm, to be used in the environment of the flow formulation implemented via the pseudo-concentrations technique.

We validated the numerical results obtained using the new algorithm by comparing the finite element predictions with results of industrial tests.

A future task to be developed in order to improve the simulation of the piercing process is the characterization of the Mannesmann effect. To attain this objective it is necessary to identify the physical mechanism that is accountable for the central hole formation and to develop a mathematical formulation to simulate it.

Acknowledgement 1 *We gratefully acknowledge the support of TENARIS for this research.*

A Implementation details for level 2

In this Appendix we discuss the heuristic logic implemented for Level 2.

A.1 Opening of the active segments under tensile normal stresses

We define the head of an arc as the first (1/3) of its active segments, starting from $J1$ (see Fig. 6); the rest of the active segments constitute the tail of the arc.

If in the head of an arc we find a number of active segments under tensile normal stress we deactivate only one of those segments at a time, starting from the first one. If in the tail of an arc we find a number of active segments under tensile normal stress we deactivate them but without deactivating at a time more than a predefined NTS number of segments.

A.2 Preventing material penetration through the active arc heads

After obtaining the $c2$ -distribution, at each active arc head we can find one of the three possibilities described in Fig. 30.

For each case we proceed as indicated below in Table A.I.

Case in Fig. 30	Action
a	Activate two arc segments
b	Close the contacts in the arc segment ($J1 - 1 \longleftrightarrow J1$)
c	Open the contacts in the first active segment

Table A.I. Arc heads strategy

Please notice that:

- The $c2$ -distribution is only used to analyze the contacts.
- The actual and fictitious materials are defined using the c -distribution, which is only actualized in the third level.

In Fig. 31 the active segments shall be modified in any of the cases where $|dc| > DTOL$.

For case (a) in table A.I we look through all the segments and make a list of the nodes that are candidates to be activated; the candidates are those nodes with outgoing velocity and $dc > DTOL$. From all the candidate nodes we activate the last two nodes (the ones with the largest values of J in Fig. 6)

The tolerance $DTOL$ is a function of the mesh size, a very small $DTOL$ will produce an unstable algorithm while a very large one will produce an inaccurate result (see section 5.2.1)

A.2.1 Measurement of the distance to the contact (dc)

For the previous step it is very relevant to measure dc as accurately as possible, and this is not a simple task. For this purpose in the METFOR implementation we define for each contact node, along the normal velocity direction “sensor points” that, using either a linear or quadratic interpolation, allow the definition of the point with $c2 = 0$ along that direction (see Fig. 32)

A.3 Flow direction correction at the active arc tails exit

In Fig. 33 we define for each arc the angles α (related to the mesh definition) and β (determined by the actual velocity field). If,

$$\begin{aligned} \beta &> f^\alpha \alpha \\ 0.5 &\leq f^\alpha \leq 1.5 \end{aligned}$$

we add a node to the active segment tail.

A.4 Prevention of cyclic contact conditions

There are cases in which a converged solution cannot be reached because the iterative procedure describes a loop of the kind pictured in the following table:

Iteration	Contacts in Group A	Contacts in Group B
1	Open	Close
2	Close	Open
3	Open	Close
...
...

Table A.II. Contact conditions loop

For breaking down these loops we have introduced a routine that:

- Identifies if a given “*open-close-open*” pattern is repeated.
- Identifies the best of the two repeated situations (e.g. the one with less interference between the actual material and the forming tools).
- Blocks the occurrence of the alternative contacts situation.

The blocking is released if at the iteration following the blockage the program does not try to reach the forbidden pattern.

References

- [1] E.N.Dvorkin, M.A.Cavaliere and M.B.Goldschmit, "Finite element models in the steel industry. Part I: simulation of flat product manufacturing processes", *Computers & Structures*, **81**, pp.559-573, 2003.
- [2] O.C.Zienkiewicz, P.C.Jain and E.Oñate, "Flow of solids during forming and extrusion: some aspects of numerical solutions", *Int.J.Solid Struct.*, **14**, pp.15-28, 1977.
- [3] E.Thompson and R.E.Smelser, "Transient analysis of forging operations by the pseudo-concentrations method", *Int .J. for Num. Methods in Engng.* , **25**, pp.177-189, 1988.
- [4] E.Thompson, "Use of the pseudo-concentrations to follow creeping viscous flows during transient analysis", *Int. J. for Num. Methods in Fluids*, **6**, pp.749-761, 1986.
- [5] E.N.Dvorkin and R.G.Toscano, "A new rigid-viscoplastic model for simulating thermal strain effects in metal forming processes", *Int. J. Numerical Methods in Engng.*, **58**, pp.1803-1816, 2003.
- [6] M.D.Demarco and E.N.Dvorkin, "Modelling of metal forming processes: implementation of an iterative solver in the flow formulation", *Computers & Structures*, **79**, pp.1933-1942, 2001.
- [7] M.A.Cavaliere, M.B.Goldschmit and E.N.Dvorkin, "Finite element simulation of the steel plates hot rolling process", *Int. J. Numerical Methods in Engng.*, **52**, pp.1411-1430, 2001.
- [8] M.A.Cavaliere, M.B.Goldschmit and E.N.Dvorkin, "Finite element analysis of steel rolling processes", *Computers & Structures*, **79**, pp.2075-2089, 2001.
- [9] E.N.Dvorkin, M.A.Cavaliere, M.B.Goldschmit and P.M.Amenta, "On the modeling of steel product rolling processes", *Int.J.Forming Processes (ESAFORM)*, **1**, pp.211-242, 1998.
- [10] E.N.Dvorkin, M.B.Goldschmit, M.A.Cavaliere, P.M.Amenta, O.Marini and W.Stroppiana, "2D finite element parametric studies of the flat rolling process", *J. of Materials Processing Technology*, **68**, pp.99-107, 1997.
- [11] E.N.Dvorkin, M.A.Cavaliere and M.B.Goldschmit, "A three field element via augmented Lagrangian for modeling bulk metal forming processes", *Computational Mechanics*, **17**, pp.2-9, 1995.
- [12] E.N.Dvorkin and E.G.Petöcz, "An effective technique for modeling 2d metal forming processes using an Eulerian formulation", *Engng. Computations*, **10**, pp.323-336, 1993.

- [13] D.Demarco and E.N.Dvorkin, “An Eulerian finite element formulation for modeling stationary finite strain elastic deformation processes”, *Int. J. Numerical Methods in Engng.*, **62**, pp.1038-1063, 2005.
- [14] P.Perzyna, “Fundamental problems in viscoplasticity”, *Advances in Applied Mechanics*, **9**, Academic Press, 1966.
- [15] A.N.Brooks and T.J.R. Hughes, “Streamline upwind Petrov-Galerkin formulations for convection dominated flows with particular emphasis on the incompressible Navier-Stokes equation”, *Comp. Meth. Appl. Mech. Engrg.*, **32**, pp. 199-259, 1982.
- [16] T.J.R Hughes and A.N. Brooks, “A theoretical framework for Petrov-Galerkin methods with discontinuous weighting functions: Application to the streamline-upwind procedure”, *Finite Element Fluids*, Chapter 3, pp. 47-65, John Wiley & Sons, 1982.
- [17] O.C.Zienkiewicz and R.L.Taylor, *The Finite Element Method*, McGraw-Hill, 1989.
- [18] T.Belytschko, W.K.Liu and B.Moran, *Nonlinear Finite Elements for Continua and Structures*, John Wiley and Sons, Chichester, 2000.
- [19] W.A.Backofen, *Deformation Processing*, Addison-Wesley, Reading MA, 1972.
- [20] E.N.Dvorkin, “On the convergence of incompressible finite element formulations: the Patch Test and the Inf-Sup condition”, *Engng. Computations*, **18**, pp.539-556, 2001.
- [21] G.E.Dieter, *Mechanical Metallurgy*, McGraw Hill, 1986.
- [22] M.A.Cavaliere, G.Gómez, J.I.Gazzarri, T.E.Pérez and E.N.Dvorkin, “Experimental procedure for determining true stress - true strain curves for steels in the high temperature range and under controlled deformation rate”, *Proceedings ECCOMAS 2000 (European Congress on Computational Methods in Applied Sciences and Engineering) - COMPLAS VI (Sixth Int. Conf. on Computational Plasticity)*, Barcelona, CIMNE, 2000.
- [23] R.Codina and O.Soto, “A numerical model to track two-fluid interfaces based on a stabilized finite element method and the level set technique”, *Int. J. Numerical Methods in Fluids*, **4**, pp.293-301, 2002.
- [24] K.J.Bathe, *Finite Element Procedures*, Prentice Hall, 1996.
- [25] J.Kajtoch and S.Urbanski, “Distribution of metal torsion in a rotary piercing mill”, *Steel Research*, **65**, pp.382-389, 1994.
- [26] O.Pejcoch, “The workability of steels in the rolling of pipes”, *Sbornik Vsb Ostrava*, **25**, pp.171-187, 1979.

- [27] T.Z.Blazynski, *Metal Forming: Tool Profiles and Flow*, John Wiley & Sons, New York, 1976.
- [28] A. Tselikov, *Stress and Strain in Metal Rolling*, MIR Publishers, Moscow, 1967.
- [29] C.F.Zorowski and R. L. Holbrook, "Influence of Mill Setup on Hollow Geometry Produced by Rotary Piercing", *Advances in Machine Tool Design and Research*, Part 2, pp. 1041-1059, Pergamon Press, 1967.
- [30] T.Z.Blazynsky and I.M.Cole, "An analysis of redundant deformation in rotary piercing", *Proc. Instn. Mech. Engrs.*, **178-1**, No. 33, pp.867-893, 1964.
- [31] E. Erman, "The effect of processing parameters on the propensity for central fracturing in piercing", *J. Applied Metalworking*, **4**, pp.331-341, 1987.
- [32] P.K.Teterin and Yu.F.Luzin, "On the mechanism of metal rupture during cross rolling", *Stal*, **10**, pp.758-760, 1960.
- [33] P. Marino and A. Pignotti, "On-line Model for Controlling an Industrial Rotary Reheating Gas Furnace", *Proceedings of the 4th European Conference on Industrial Furnaces and Boilers*, Espinho, Portugal, 1-4 April 1997.
- [34] J.Yang, G.Li, W.-T.Wu, K.Sawamiphakdi and D.Jin, "Process modeling for rotary tube piercing application", *Proceedings Materials Science & Technology Conference*, AIST-TMS, New Orleans, 2004.
- [35] K.Komori and M.Suzuki, "Simulation of deformation and temperature in piercing rolling", *Proceedings European Congress on Computational Methods in Applied Sciences and Engng. (ECCOMAS 2004)*, Ed. P.Neittaanmäki et al, Jyväskylä, Finland, 2004.
- [36] J.Pietsch and P.Thieven, "FEM simulation of the rotary tube piercing process", *MPT International*, April 2003.
- [37] Y.Wada, K.Yamada, S.Hamauzu and S.Uchida, "Three-dimensional analysis of helical rolling of bar and pipe using rigid-plastic finite element method", *Numiform '98 - Simulation of Materials Processing: Theory, Methods and Applications*, Ed. J.Huétink and F.P.T.Baaijens, Balkema, Rotterdam, 1998.
- [38] K.Mori, H.Yoshimura and K.Osakada, "Simplified three-dimensional simulation of rotary piercing of seamless pipe by rigid-plastic finite-element method", *J. of Materials Processing Technology*, **80-81**, pp.700-706, 1998.
- [39] M.A.Cavaliere, D.A.Berazategui, M.B.Goldschmit, E.N.Dvorkin, L.Montelatici and D.Wolter, "Modeling of the piercing process: preliminary results", *Proceedings of the 14th. rolling conference*, I.A.S., San Nicolás, Argentina, November 2002.

- [40] L.Montelatici, B.Scarabelli, S.Tosato, D.Wolter and E.N.Dvorkin, “Full-scale experimental determination of the material deformation in a piercing mill on a seamless tubes rolling line”, *Proceedings of the 14th. rolling conference*, I.A.S., San Nicolás, Argentina, November 2002.
- [41] A.P.Assanelli, R.G.Toscano, D.H.Johnson and E.N.Dvorkin, “Experimental / numerical analysis of the collapse behavior of steel pipes”, *Engng. Computations*, **17**, pp.459-486, 2000.

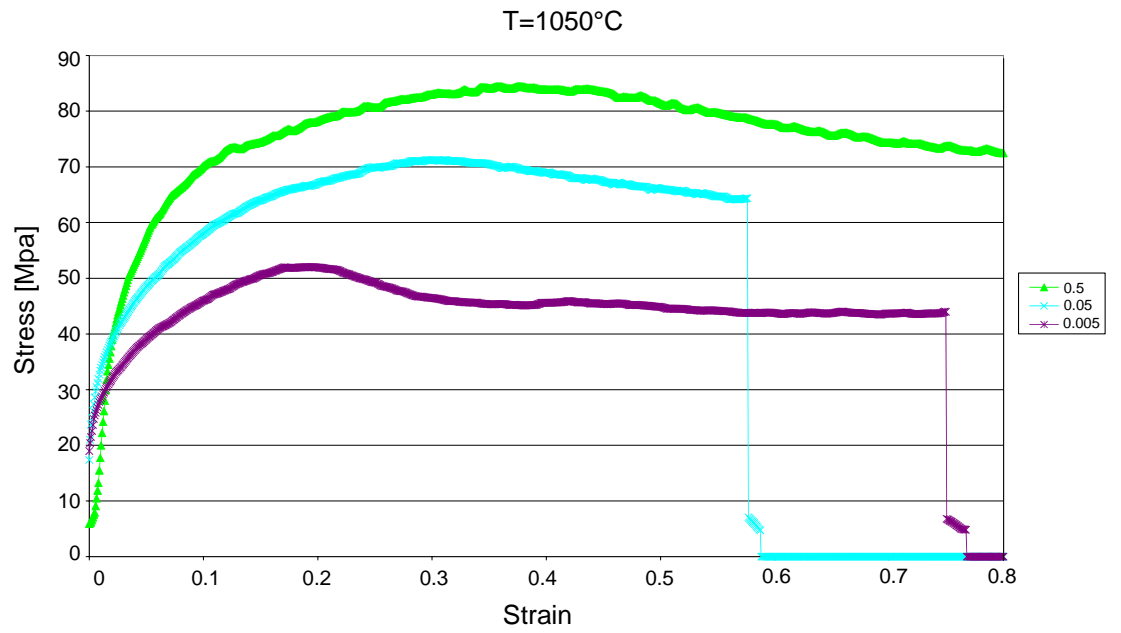


Figure 1: Compression tests performed at 0.005, 0.05 and 0.5 1/sec and at elevated temperature

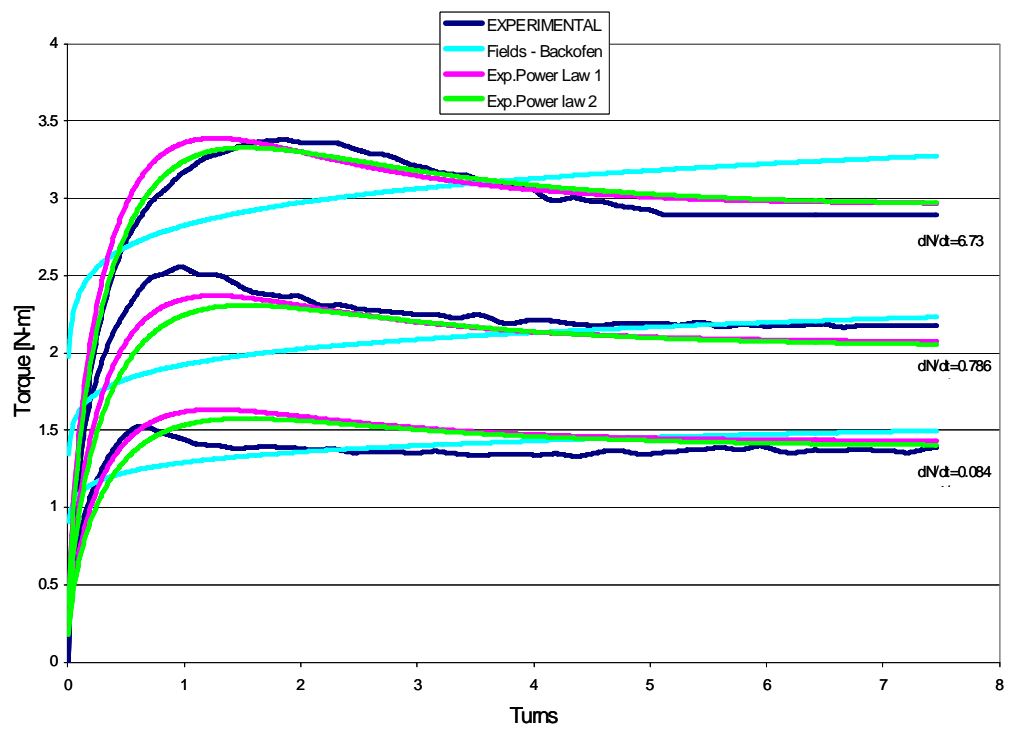


Figure 2: Torque - turn curves at $1050^{\circ}C$

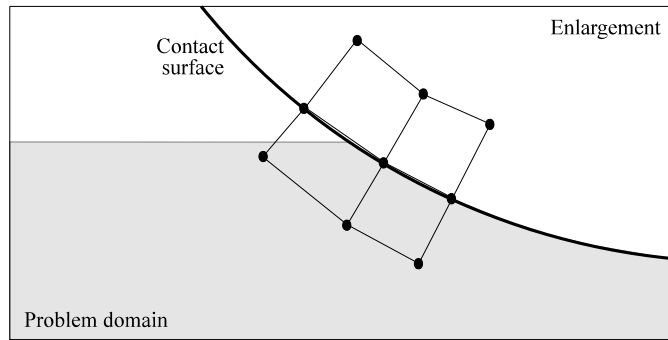


Figure 3: Mesh extension to impose a c -boundary condition on the in-coming material

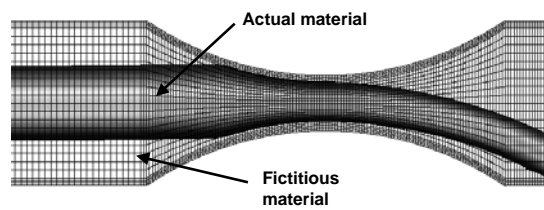


Figure 4: 2D model of non-symmetric rolling of steel plates using the pseudo-concentrations technique

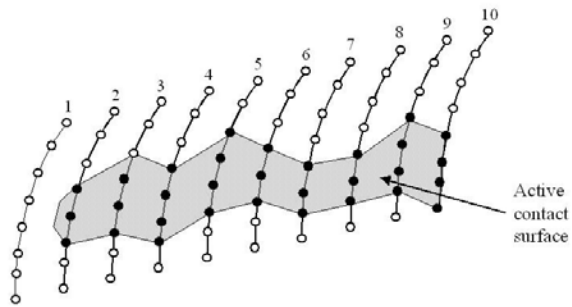


Figure 5: Contact arcs on a forming tool

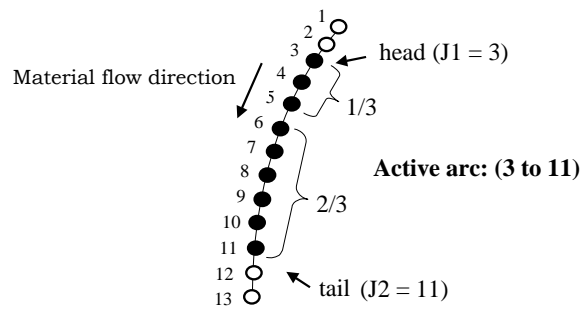


Figure 6: A contact arc

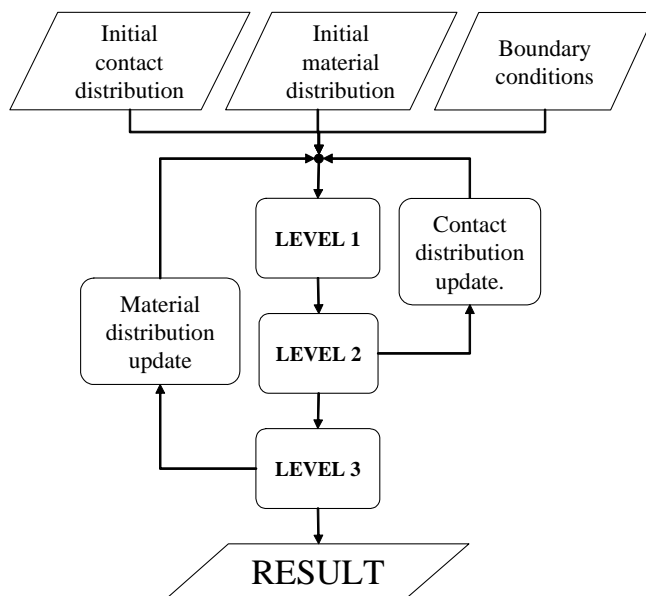


Figure 7: Iterative cycle

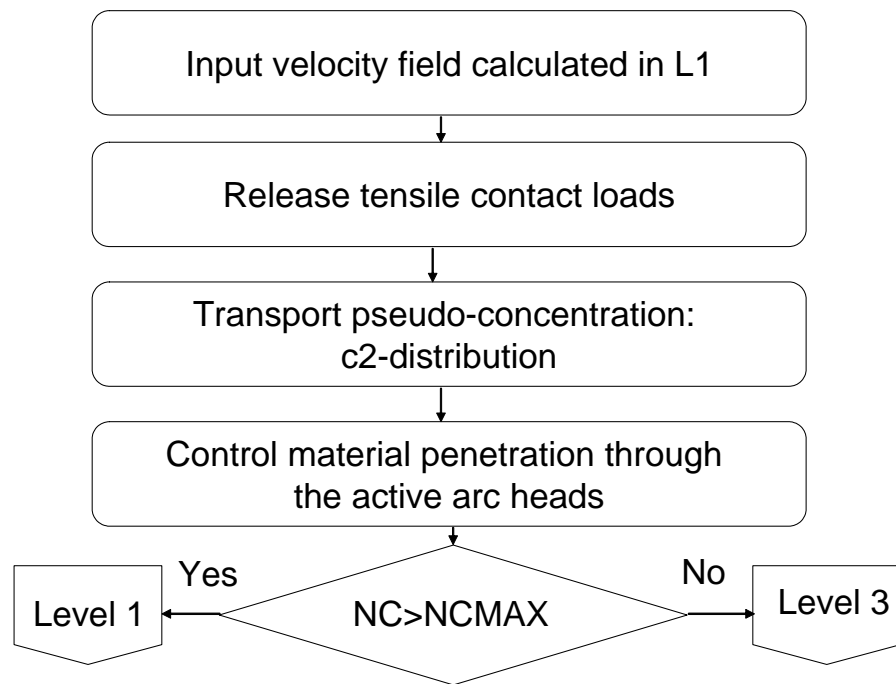


Figure 8: Level 2 of the iterative cycle

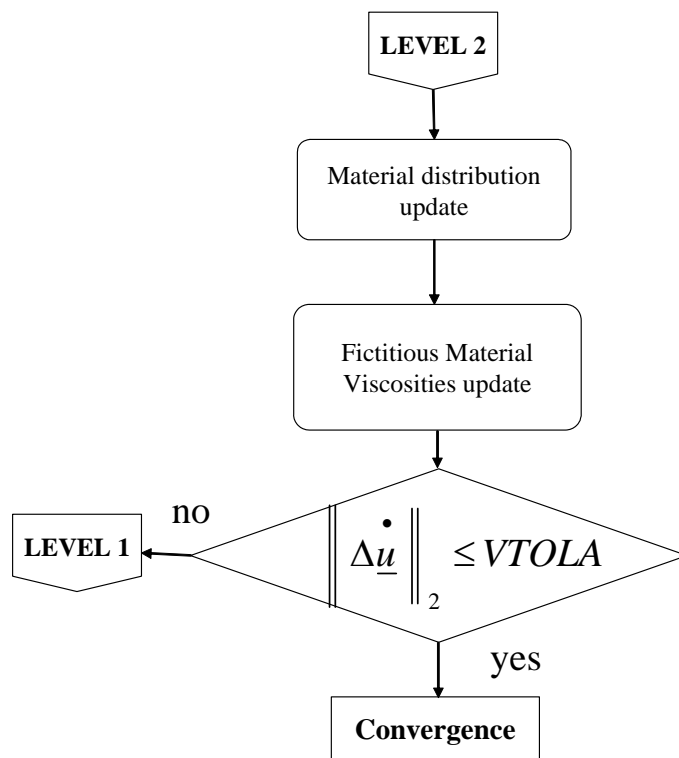


Figure 9: Level 3 of the iterative cycle

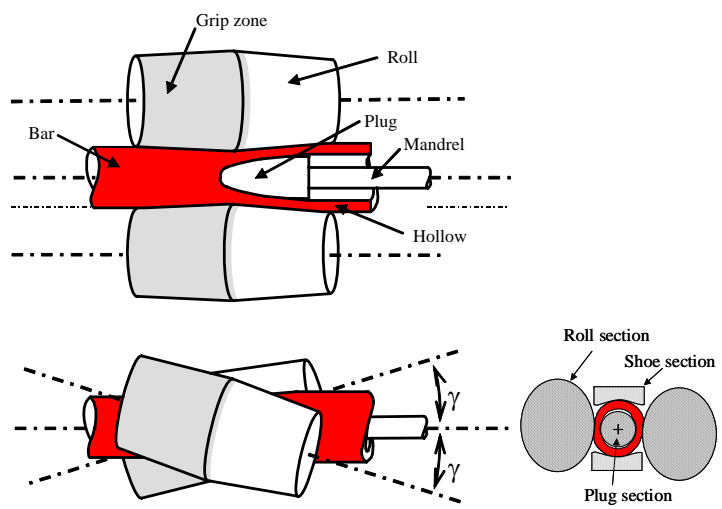


Figure 10: Mannesmann piercing process

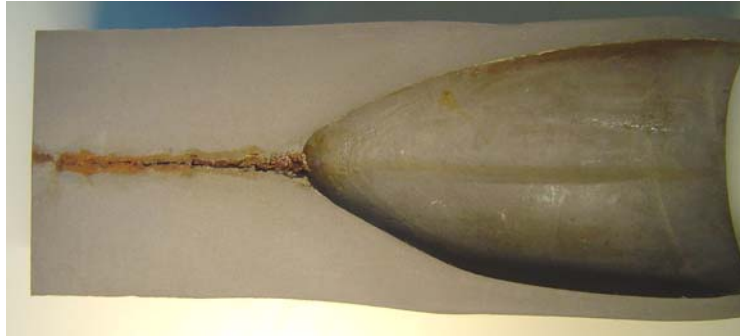


Figure 11: The Mannesmann effect

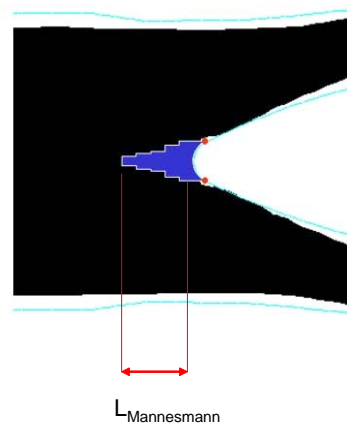


Figure 12: Damaged cone used to “approximate” the Mannesmann effect (in blue)




	Profile scheme	Bar diameter
Case 1		395 mm
Case 2		395 mm
Case 3		215 mm

Figure 13: Cases to be analyzed for the validation of the finite element model

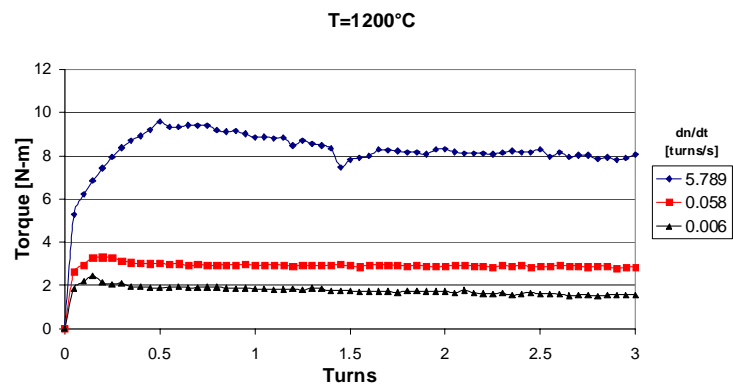


Figure 14: Torsion tests of the steel used for the model validation

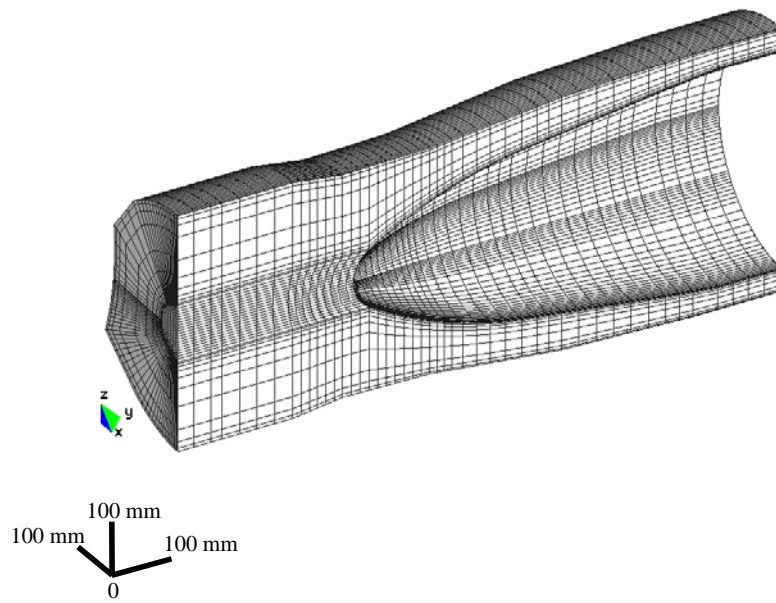


Figure 15: Finite element mesh used for case 1 (314,097 d.o.f)

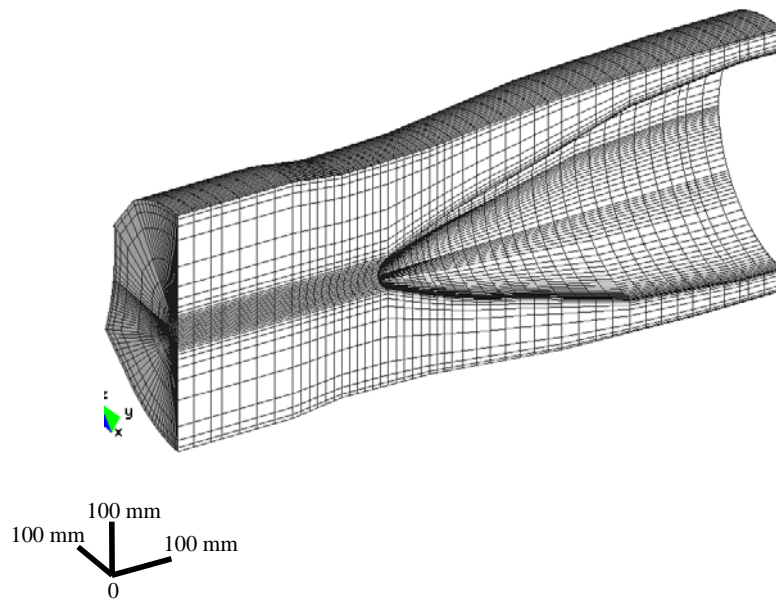


Figure 16: Finite element mesh used for case 2 (327,444 d.o.f)

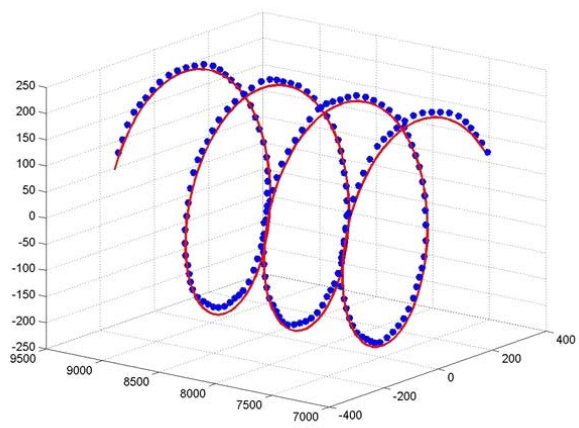


Figure 17: Torsion helix

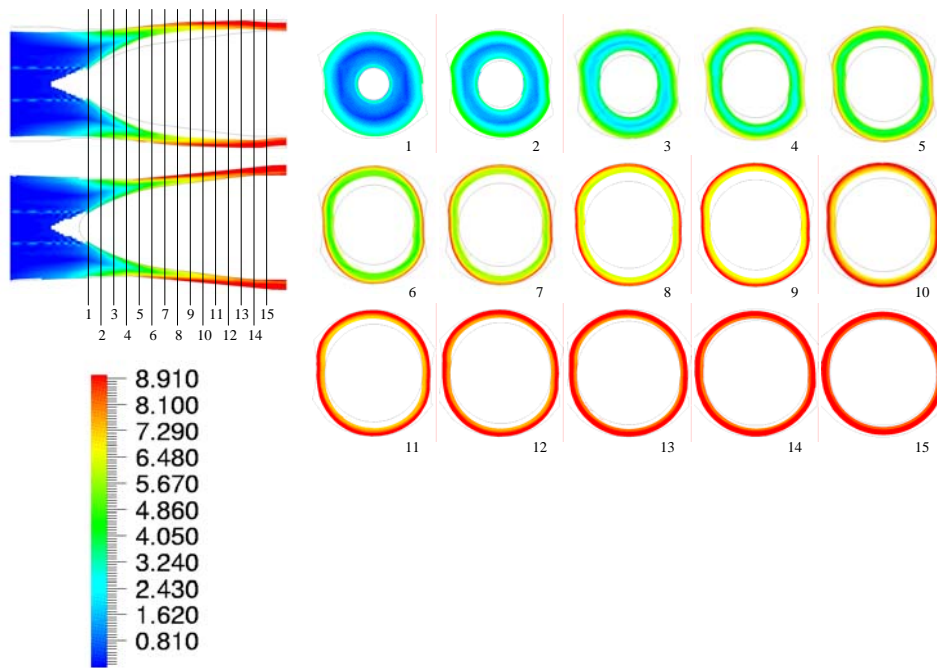


Figure 18: Accumulated effective viscoplastic strain for plug design # 1. The two axial sections are: (a) top one through the shoes (b) bottom one through the rolls

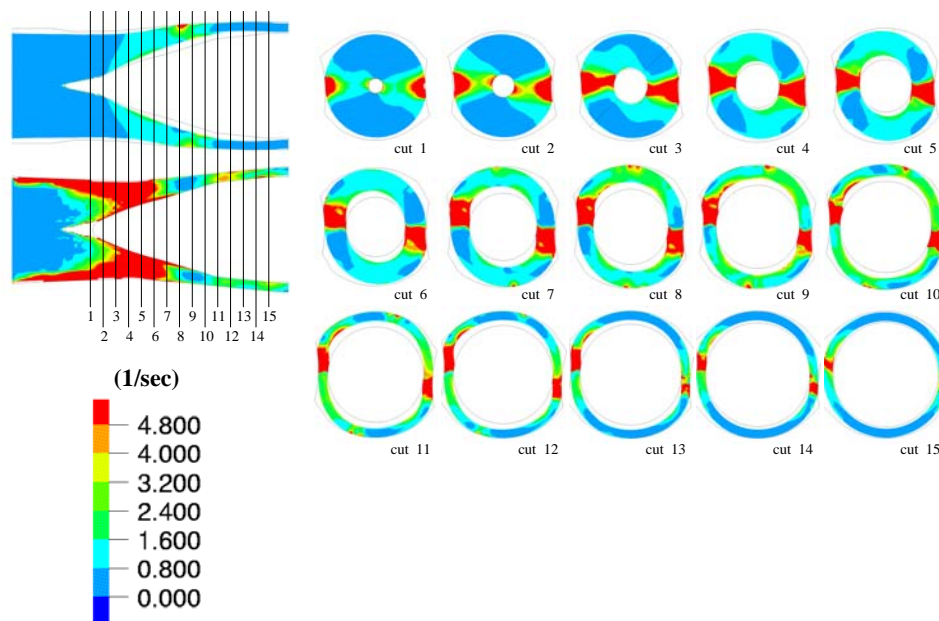


Figure 19: Viscoplastic strain rates for plug design # 2. The two axial sections are: (a) top one through the shoes (b) bottom one through the rolls

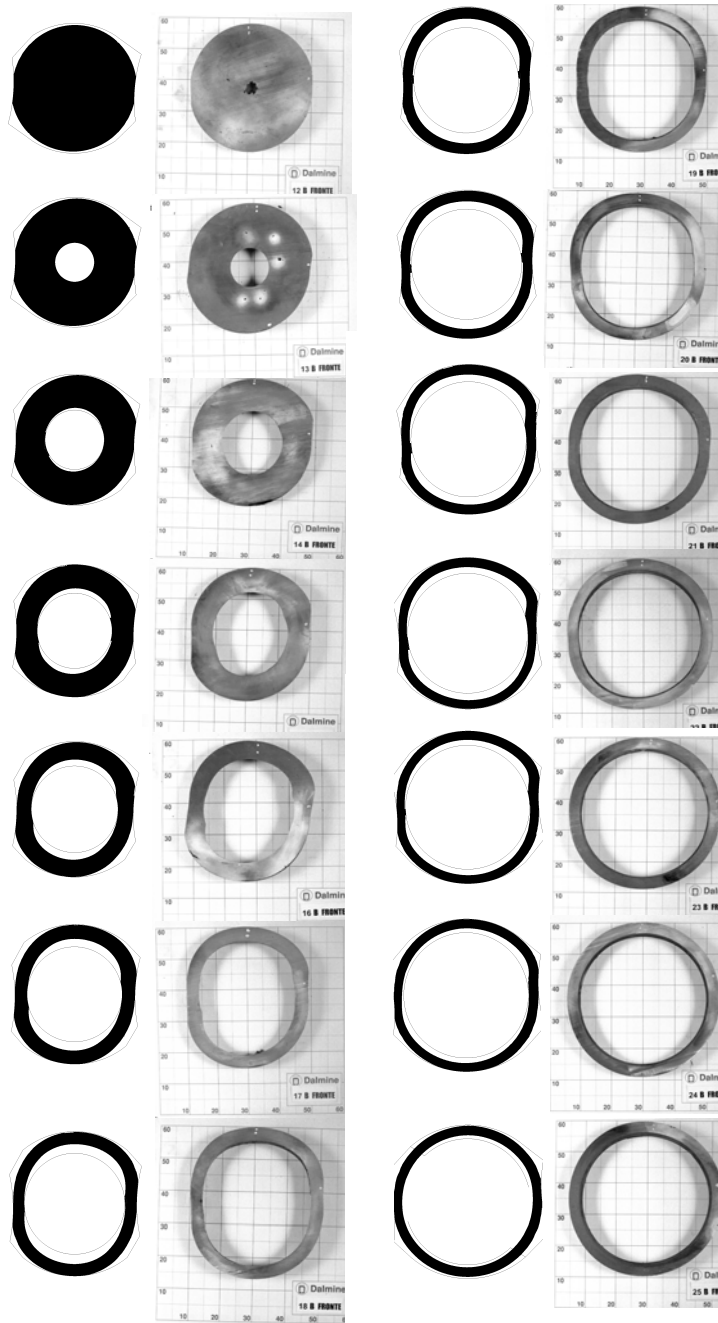


Figure 20: Plug profile # 1. Comparison between the numerical predicted and experimental cross sections

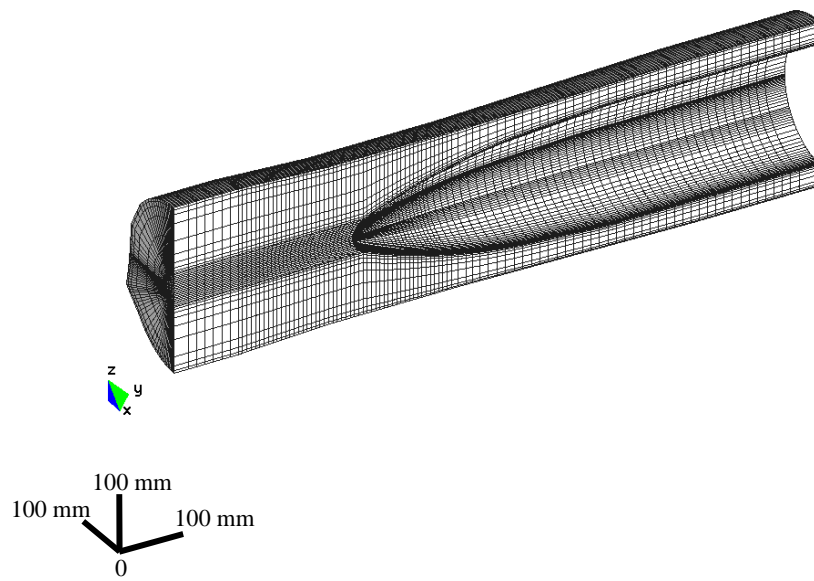


Figure 21: Finite element mesh used for case 3 (660,117 d.o.f)

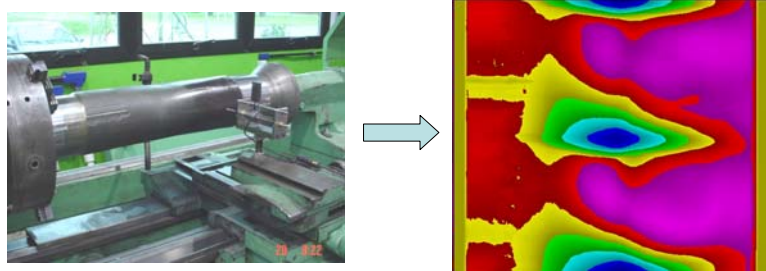


Figure 22: Mapping of the outer surface

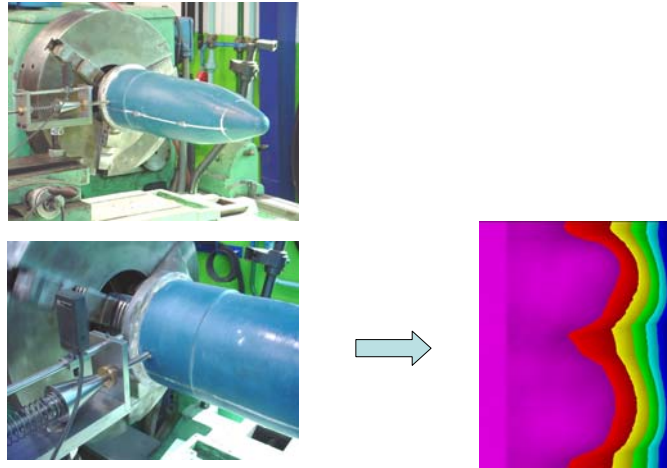


Figure 23: Mapping of the inner surface via a resin replica

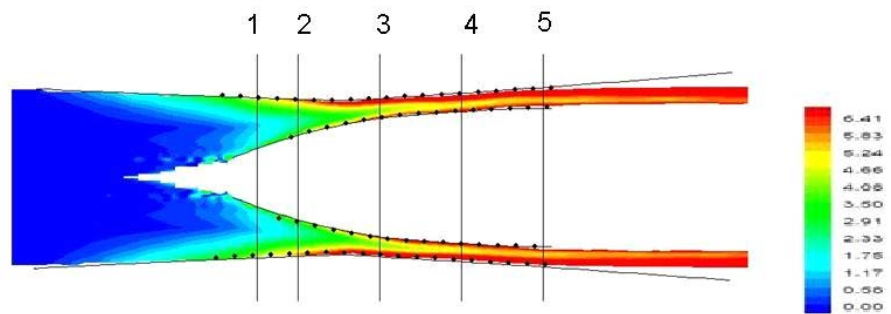


Figure 24: Section through the rolls. The color map indicates the equivalent plastic strain and the dots the mapped data.

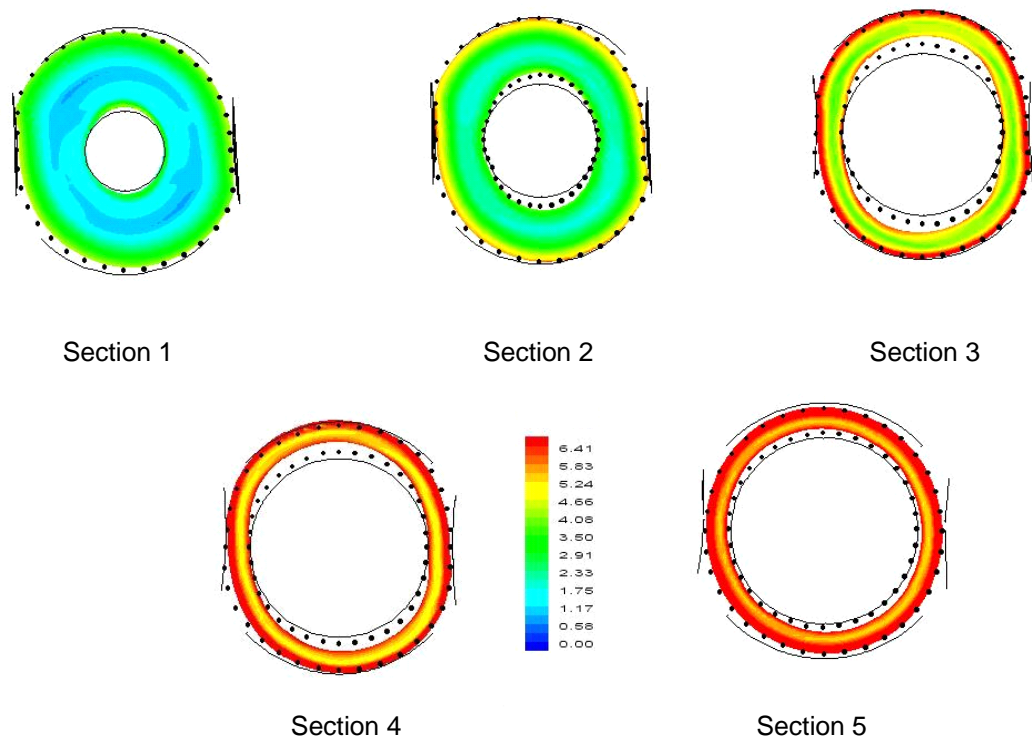


Figure 25: Transversal sections (indicated in the previous figure). The color map indicates the equivalent plastic strain and the dots the mapped data

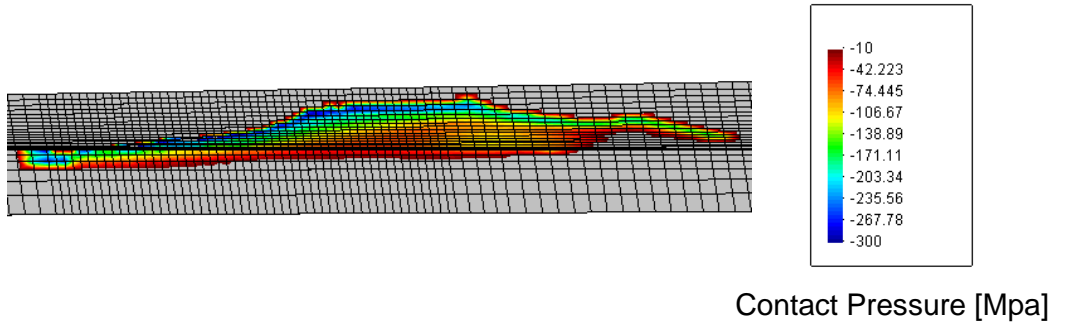
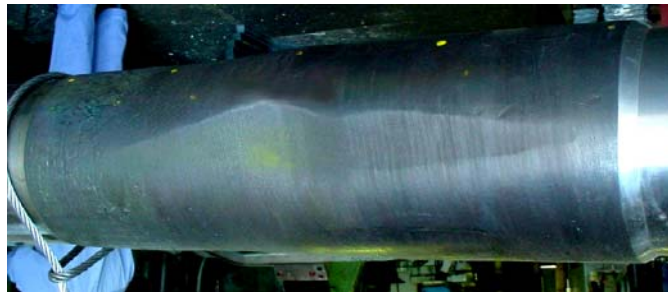


Figure 26: Actual and finite element predicted contact area rolls-bar

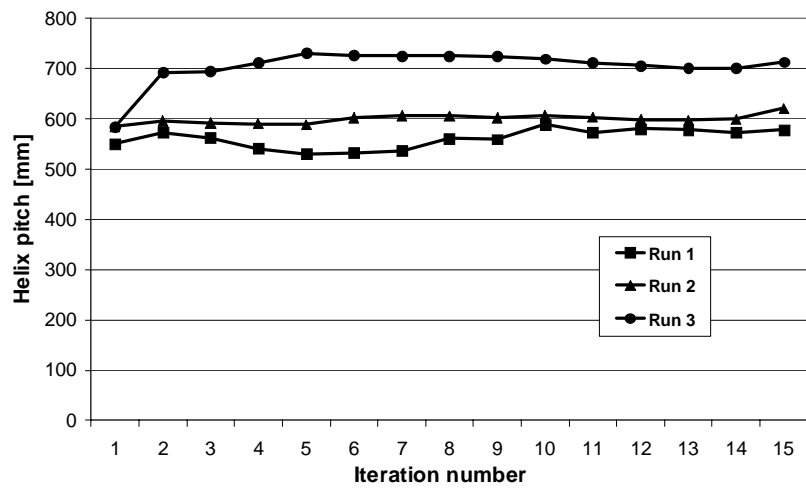


Figure 27: Behavior of the iterative algorithm using different $DTOL$ values

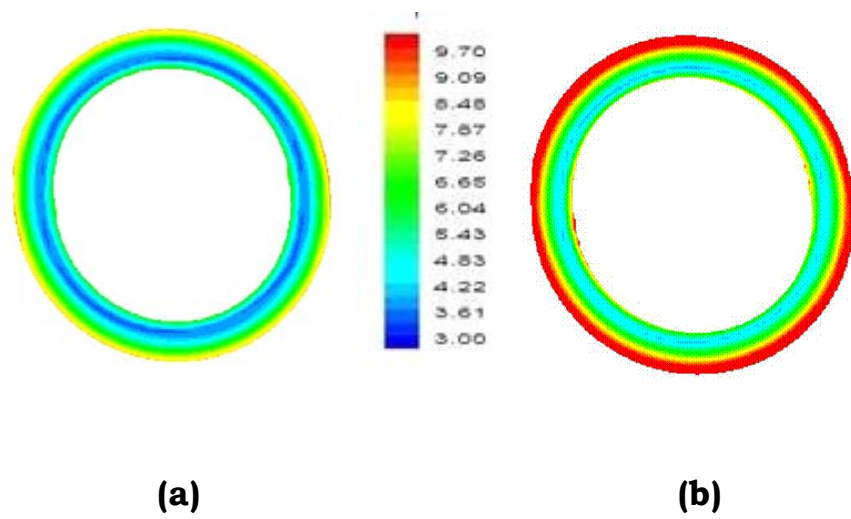


Figure 28: Equivalent viscoplastic strains in the pierced pipe (a) Case A (b) Case B

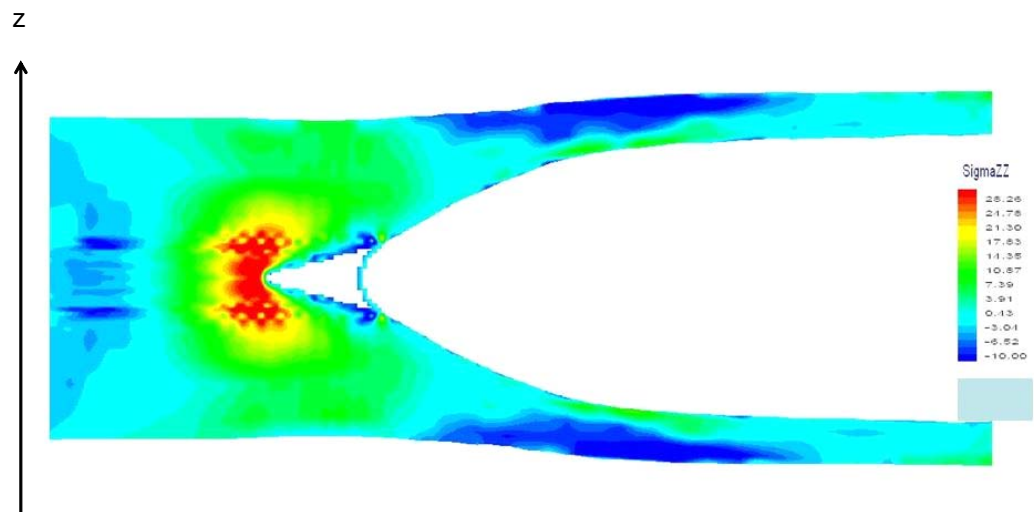


Figure 29: Stresses- zz in a section through the shoes

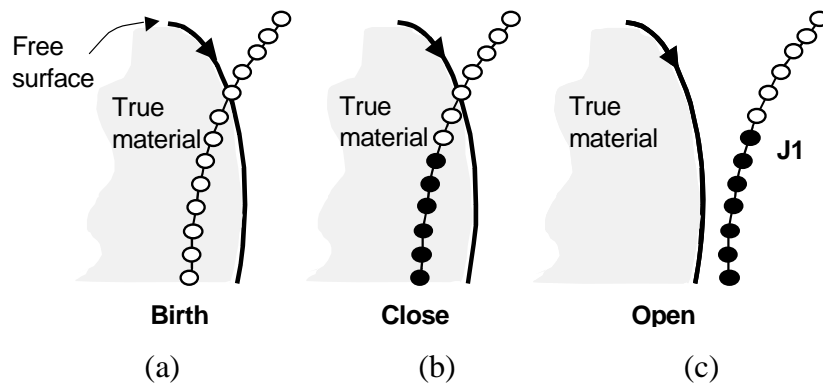


Figure 30: Different cases at the arc heads

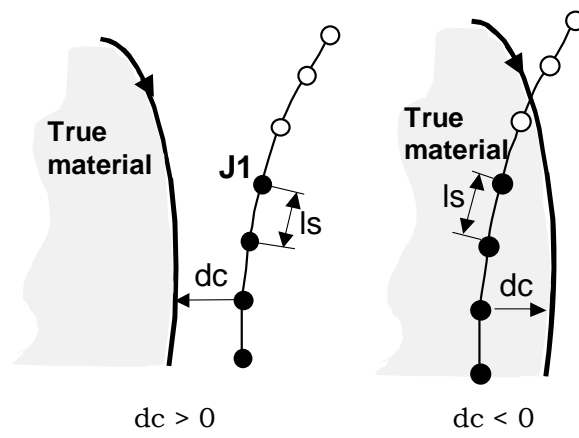


Figure 31: True material penetration or separation from the forming tool

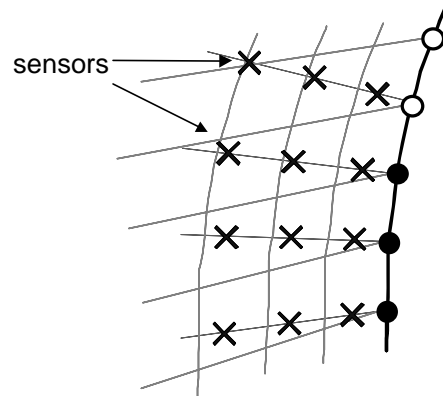


Figure 32: Sensor points

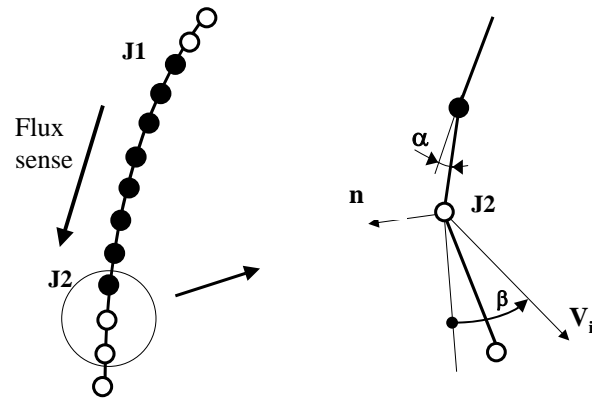


Figure 33: Material conservation at the arc tails (\underline{n} is normal to the tool surface)